Research Article Vol. 5, No. 8 / August 2018 / Optica 954

Exciting a chiral dipole moment in an achiral nanostructure

Jörg S. Eismann,[1,2] Martin Neugebauer,[1,2] and Peter Banzer[1,2,*]

[1]Max Planck Institute for the Science of Light, Staudtstr. 2, D-91058 Erlangen, Germany
[2]Institute of Optics, Information and Photonics, University Erlangen-Nuremberg, Staudtstr. 7/B2, D-91058 Erlangen, Germany
*Corresponding author: peter.banzer@mpl.mpg.de

Received 18 May 2018; revised 5 July 2018; accepted 8 July 2018 (Doc. ID 332063); published 3 August 2018

Controlling the electric and magnetic dipole moments of optical nanostructures is a fundamental prerequisite for light routing and polarization multiplexing at the nanoscale. A versatile approach for inducing tailored dipole moments is structured illumination. Here, we discuss the excitation of a chiral dipole moment in an achiral silicon nanoparticle. In particular, we make use of the electric and magnetic polarizabilities of the silicon nanoparticle to coherently excite a superposition of parallel electric and magnetic dipole moments phase-shifted by $\pm\pi/2$, which resembles the fundamental mode of a three-dimensional chiral nanostructure. We demonstrate the wavelength dependence of the excitation scheme and measure the spin and orbital angular momenta in the emission of the induced chiral dipole moments. Our results highlight the capabilities of such tunable chiral dipole emitters—not limited by structural properties—as flexible sources of spin-polarized light for nanoscopic devices.

OCIS codes: (290.5855) Scattering, polarization; (260.0260) Physical optics; (350.4238) Nanophotonics and photonic crystals; (050.5080) Phase shift; (050.4865) Optical vortices.

https://doi.org/10.1364/OPTICA.5.000954

1. INTRODUCTION

The recent experimental demonstrations of electromagnetic dipole moments induced in silicon and other high-refractive index nanoparticles highlight the importance of such structures as building blocks for novel nanophotonic devices and metasurfaces [1,2]. For example, the simultaneous and in-phase excitation of perpendicular electric and magnetic dipole moments—commonly referred to as Huygens' dipole [3]—leads to strongly directional scattering patterns, allowing for highly efficient routing and polarization multiplexing at the nanoscale [4]. Additionally, other combinations of electric and magnetic dipole moments can be achieved by providing carefully structured excitation fields [5–9].

In this paper, we study an electromagnetic dipole moment in the helicity basis [10]. Such a σ dipole consists of parallel electric and magnetic dipole moments of equal amplitudes and a relative phase of $\pm\pi/2$, leading to a well-defined helicity of ± 1 [10–12]. Furthermore, the σ dipole is equivalent to the coupled dipole moments observed for the fundamental mode of a chiral nanostructure [13–16]. In these works, the occurrence of a σ-dipole component is directly linked to the chiral geometry of the system. Here, we experimentally investigate the σ dipole for the first time by exciting it in an achiral nanoparticle with an in-phase superposition of tightly focused radially and azimuthally polarized beams. Before focusing, such a composite beam is locally, linearly polarized and carries neither spin angular momentum (SAM) nor orbital angular momentum (OAM). In the focal plane, the beam exhibits in-phase longitudinal electric and magnetic fields of equal amplitudes on the optical axis. However, because electric and magnetic polarizabilities of the particle are wavelength dependent, we obtain a superposition of phase-delayed electric and magnetic longitudinal dipole moments induced in the particle, which results in the emission of light with predominantly positive or negative helicity. Adapting the excitation wavelength, we maximize the helicity of the excited dipole by balancing the dipole moments. The excited dipoles not only result in a far-field emission carrying SAM, but also OAM occurs as a result of an azimuthal phase front. We begin with a theoretical comparison of a spinning dipole and σ dipoles. Then, we describe our experimental scheme, including the tailored excitation of a σ dipole, and, finally, we compare experimental and theoretical results and elaborate on the far-field helicity and the chirality of the excited dipole moments.

2. SPINNING AND CHIRAL DIPOLE MOMENTS

In order to emphasize the fundamental difference between a spinning dipole and the σ dipoles, on which we will mainly focus in this study, we plot corresponding radiation patterns in Fig. 1. The color code refers to the far-field helicity defined by $\sigma = (I_{\mathrm{rhc}} - I_{\mathrm{lhc}})/(I_{\mathrm{rhc}} + I_{\mathrm{lhc}})$ [17] with I_{rhc} and I_{lhc} as the intensities of the emitted right-handed circularly (rhc) and left-handed circularly (lhc) polarized fields, respectively. In Figs. 1(a)–1(c), the

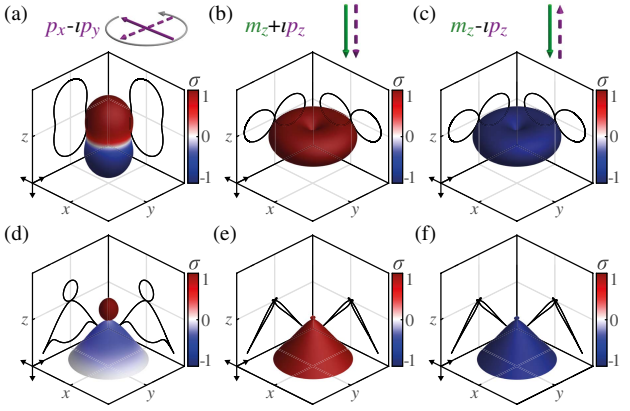

Fig. 1. Radiation patterns of a spinning dipole and σ dipoles. The color code corresponds to the helicity σ. The upper row shows the emission in free-space, the lower row shows the emission of the same dipoles placed 88 nm above a glass substrate ($n_G = 1.53$). (a), (d) Spinning dipole with dipole moment $\mathbf{p} = p_0(1, -\imath, 0)$. (b), (e), (c), (f) σ dipoles with dipole moments $\mathbf{p} = p_0(0, 0, \pm\imath)$ and $\mathbf{m} = m_0(0, 0, 1)$.

dipoles are emitting in free-space, where (a) shows the spinning electric dipole with $\mathbf{p} = p_0(1, -\imath, 0)$. Figures 1(b) and 1(c) depict two σ dipoles with positive and negative helicities defined by a combination of $\mathbf{p} = p_0(0, 0, \pm\imath)$ and $\mathbf{m} = m_0(0, 0, 1)$. Here, $\mathbf{p}$ and $\mathbf{m}$ refer to the electric and magnetic dipole moments in Cartesian coordinates with $p_0 = m_0/c_0$. For our geometry, where we only use z-oriented dipoles, the σ dipoles can be expressed in a very compact form by using a notation that combines electric and magnetic dipole moments [18]:

$$\boldsymbol{\sigma}_{\pm} = A^{\pm}\begin{pmatrix} \pm\imath \\ 1 \end{pmatrix}, \tag{1}$$

where the upper entry inside the brackets refers to the electric z-dipole moment, the lower entry refers to the magnetic z-dipole moment, and $A^{\pm}$ are the overall amplitudes of the dipoles (in Ref. [18], the combined vector represents the general case of three electric and three magnetic dipole components). For the regular spinning dipole in Fig. 1(a), the polarization of the emitted light is anisotropic with different signs of helicity in the upper and lower half-space [19]. The average helicity is exactly zero. In contrast, for the two σ dipoles in Figs. 1(b) and 1(c), the helicity is isotropic with an average of exactly ± 1 [12].

In our experiment described below, the dipole emitter will be sitting on a dielectric interface for practical reasons. The dielectric interface near the emitter strongly alters the emission patterns (see Ref. [20] and references therein), enhancing the emission to the optically denser medium (here, lower half-space with $z > 0$). The far field emitted into the substrate can be calculated utilizing a plane-wave decomposition following Refs. [9,21]. In this regard, we make use of the fact that any combination of z-oriented dipoles can be written as a superposition of the two σ dipoles with their complex amplitudes $A^{\pm}$ introduced in Eq. (1). With these amplitudes, the emitted far field of z dipoles can be written as

$$\begin{bmatrix} E_p \\ E_s \end{bmatrix}(k_x, k_y) \propto C\hat{\mathbf{T}}\left[A^{+}\begin{pmatrix} -\imath \\ 1 \end{pmatrix} + A^{-}\begin{pmatrix} \imath \\ 1 \end{pmatrix}\right], \tag{2}$$

where we express the far field in the transverse magnetic (E_p) and transverse electric (E_s) polarization basis, and $C = \frac{k_\perp}{k_0}[(k_0^2 n_G^2 - k_\perp^2)^{1/2}/k_z] \cdot \exp(\imath k_z d)$. Moreover, $k_0 = 2\pi/\lambda$ is the wave number in the upper half-space, c_0 is the vacuum speed of light, $k_\perp = (k_x^2 + k_y^2)^{1/2}$ is the transverse wave number, d is the distance of dipolar emitter to the interface, and the matrix $\hat{\mathbf{T}}$ contains the Fresnel transmission coefficients t_s and t_p [21]:

$$\hat{\mathbf{T}} = \begin{pmatrix} t_p & 0 \\ 0 & t_s \end{pmatrix}. \tag{3}$$

In Figs. 1(d)–1(f), we show the far fields of the aforementioned dipoles, but they are now positioned $d = 88$ nm above an air–glass interface with the refractive index of the glass substrate $n_G = 1.53$, adapted to the experiment described later. The far fields of the σ dipoles in Figs. 1(e) and 1(f), in particular, the fields emitted into the lower half-space ($z > 0$), are calculated with Eq. (2), where either A^+ or A^- is set to zero, respectively. Because of the substrate, the average helicity does not reach values of ± 1 (in contrast to free-space), but it is typically slightly lower because of the Fresnel coefficients breaking the dual symmetry of the system [12].

3. TAILORED EXCITATION SCHEME

Our intention is the tailored excitation and verification of σ-dipole moments inside a spherical silicon particle. For this purpose, we first design an excitation field capable of inducing electric and magnetic dipole moments, which are oriented parallel and have a phase difference of $\pi/2$. For paraxial beams, this is very difficult to achieve, because there the transverse electric and magnetic fields are perpendicular to each other, and the longitudinal fields are substantially weaker [21]. One possible solution can be realized by tightly focusing a superposition of radially and azimuthally polarized beams, which exhibit purely z-polarized electric and magnetic fields on the optical axis, respectively [5,22]. To achieve the desired relative phase between the electric and magnetic dipole moments, the inherent properties of the silicon particle can be utilized. Due to the complex electric and magnetic polarizabilities of the particle, a wavelength dependent phase shift between the fields and the resulting dipole moments is introduced [6].

Accordingly, for our experimental implementation, we utilize a superposition of radially and azimuthally polarized beams of equal amplitudes—a so-called spiral polarization beam—and focus it tightly. On the left of Fig. 2(a), the local polarization distribution of the incoming paraxial beam before focusing is sketched for the electric and magnetic fields with purple and green arrows. The calculated focal field distributions for a wavelength of 640 nm are depicted on the right of Fig. 2(a) with the corresponding phases plotted as insets. The overall spot size in the focal plane is approximately 880 nm (full width at half-maximum). As can be seen, on the optical axis, the electric and the magnetic fields are parallel, z-polarized, and in-phase. In contrast, all transverse field components are antisymmetric with respect to the optical axis and, therefore, cross zero on-axis. This implies that no transverse dipole moments can be excited [5]. Consequently, the induced dipole moments at this position can be approximated as $p_z = \alpha^e E_z$ and $m_z = \alpha^m H_z$, where α^e and α^m are complex polarizabilities, describing the excitation of the corresponding dipoles by electromagnetic fields [18]. It is important to emphasize the absence of any magnetoelectric or chiral terms in the polarizability, which describes a coupling of electric and magnetic dipoles. The symmetries of a spherical structure do not allow for such

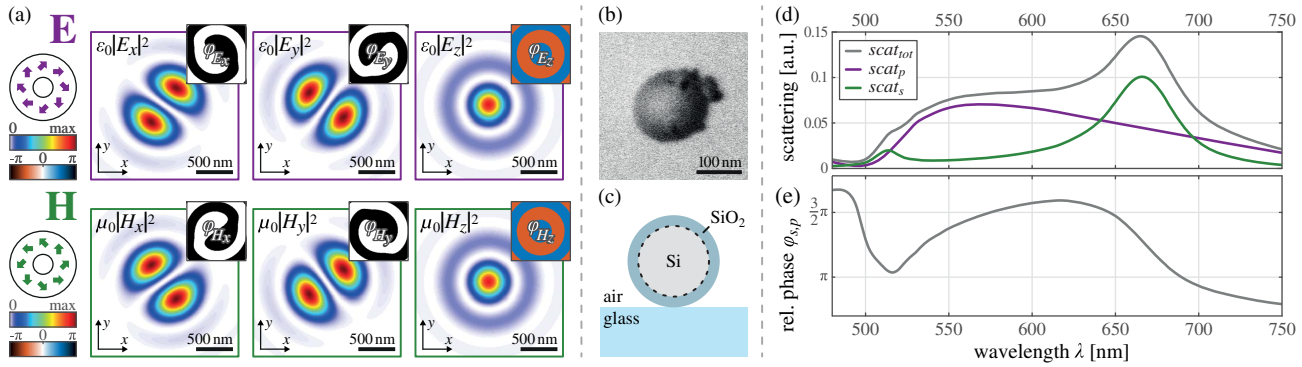

Fig. 2. (a) Spiral polarization beam. The polarization distributions of the electric and magnetic fields before focusing are depicted on the left by purple and green arrows, respectively. The field plots show the calculated electric and magnetic intensity components of the tightly focused beam in the focal plane at 640 nm. The phases are shown as insets. (b) Scanning electron microscope image of the nanoparticle, used in the experiment. (c) Sketch of the system utilized for FDTD simulation. The particle has a crystalline silicon core with radius $r_{Si} = 84$ nm, a silicon dioxide (SiO_2) shell of thickness $\delta = 4$ nm, and it is placed on an air–glass interface. (d) Total intensity (gray line) scattered into the angular region defined by $0.92 \leq k_\perp/k_0 \leq 1.28$ (glass half-space), retrieved from FDTD simulations. The purple and green lines depict the decomposition into *p*- and *s*-polarized intensities. (k) Relative phase $\varphi_{s,p}$ between the scattered fields E_s and E_p.

interaction terms, which would be present for a chiral nanostructure or a bianisotropic particle [18,23].

Next, we discuss the optical response of the chosen silicon nanoparticle, similar to those used in Refs. [5,6]. A scanning electron microscope (SEM) image of the particle is shown in Fig. 2(b). We run finite difference time-domain (FDTD) simulations using the same beam parameters and far-field collection geometry as in the experiment to investigate the spectral response of the silicon nanosphere. Although we observe a small asymmetry of the particle in the SEM image, we model it as a perfectly achiral sphere with 88 nm radius, sitting on a glass substrate [see Fig. 2(c)]. Under ambient conditions, silicon naturally forms an oxide layer with a thickness of a few nanometers [24,25]. We therefore used a core–shell model for our particle with a core radius of $r_{Si} = 84$ nm, surrounded by a silicon dioxide shell of estimated thickness $\delta = 4$ nm. In Fig. 2(d), we depict the wavelength dependent intensity scattered into the glass substrate. In particular, we consider the scattered light in the angular range defined by $0.92 \leq k_\perp/k_0 \leq 1.28$, which corresponds to the angular range, where, in our experiment, the scattered light can be detected without interference with the excitation beam. The gray line represents the total intensity, while the purple and green lines correspond to the *p*- and *s*-polarized constituents. The details of the FDTD simulation regarding the analysis for Figs. 2(d) and 2(e) resembling our experiment can be found in Supplement 1.

Following Eq. (2), we see that for the chosen geometry, the far field of an electric *z* dipole is purely *p*-polarized, while for the magnetic *z* dipole it is purely *s*-polarized. Hence, we can associate the purple curve (*p*-polarized intensity) with the light scattered by the electric dipole moment, and the stronger resonance of the green curve (*s*-polarized intensity) with the light scattered by the magnetic dipole moment. The second substantially weaker resonance of the green curve corresponds to the magnetic quadrupole [5]. Since we want to excite a σ dipole, the relative phase between the magnetic and electric *z* dipole is of special interest for us. For that reason, we plot the relative phase $\varphi_{s,p}$ between the *s*- and *p*-polarized far-field components in Fig. 2(e), evaluated from the simulated data (see Supplement 1 for details). We see that in the spectral range of 640–710 nm the relative phase depends strongly on the wavelength of the incoming beam, while the *p*- and *s*-polarized scattered intensities, associated with the electric and the magnetic dipole moments, are both of comparable strength. This provides a large tuning range of the excited dipole moments. Also, in this region, the contribution of the magnetic quadrupole with its response peaking at 510 nm is completely negligible.

4. IMPLEMENTATION

As a light source for our measurement, a supercontinuum laser source was utilized with an acousto-optical tunable filter to select the desired wavelength between 480 and 710 nm with a bandwidth of approximately 2 nm. The output of the filter is guided by a single mode fiber, which provides a collimated, linearly polarized Gaussian beam at the entrance of the main setup, shown in a simplified version in Fig. 3. A more detailed description of a similar setup and its main constituents can be found in Ref. [26]. In order to verify the generation of OAM by interferometric measurements, a beam splitter is used to split the incoming beam into two parts. The main beam is converted by a *q* plate [27] of charge $-\frac{1}{2}$ and a half-wave plate into the desired spiral polarization beam, which is spatially Fourier-filtered afterwards. A microscope objective (MO) with high numerical aperture (NA) of 0.9 is used for tightly focusing the beam onto a high-refractive-index silicon nanosphere placed on a glass substrate [28]. The system is designed such that for the measured spectral range and the utilized spiral polarization beam the focal spot size remains almost constant. The glass substrate is mounted on a sample holder and attached to a three-dimensional (3D) piezo stage, allowing for precise positioning of the particle with respect to the beam. The collection of the transmitted and forward scattered light is realized by an oil-immersion-type MO with an NA of 1.3. The two MOs form a confocal alignment to provide a collimated output of the second MO. We utilize a rotatable broadband quarter-wave plate in combination with a fixed linear polarizer, which projects the light onto different polarization states in order to perform a full far-field polarization measurement (see Ref. [29]

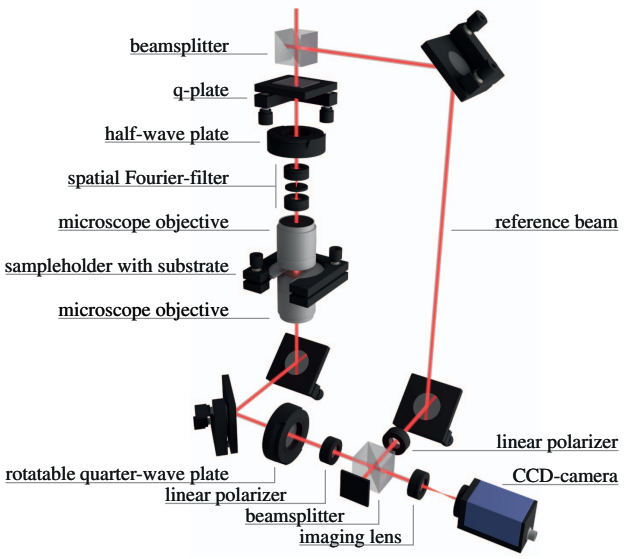

Fig. 3. Schematic draft of the measurement setup. The incoming linearly polarized Gaussian beam is split into two parts. The main beam is tailored into the desired spiral polarization beam and afterwards focused on a silicon nanostructure by a microscope objective (MO) with a numerical aperture of NA = 0.9. A second MO collects the incoming beam as well as the scattered light up to NA = 1.3. A rotatable quarter-wave plate and a linear polarizer are implemented for polarization analysis. Additionally, the reference beam can be superimposed for interferometric measurements.

for a detailed description of the technique). Thereafter, the beam passes a second beam splitter, which can be used for phase measurements by overlapping the transmitted light with the reference beam. Finally, we image the back focal plane (BFP) of the lower MO onto the CCD camera. Because the collecting MO has a higher NA than the MO used for focusing of the beam, in the angular range defined by NA = [0.9, 1.3], no contribution of the excitation field itself is found, only scattered light. This allows for investigating the type of the excited electromagnetic dipole. For the interference measurements, the linearly polarized reference beam was overlapped with the scattered light under a small angle.

5. EXPERIMENTAL RESULTS AND DISCUSSION

For the first measurement, we investigated the spectral behavior of the average helicity $\bar{\sigma} = (W_{\mathrm{rhc}} - W_{\mathrm{lhc}})/(W_{\mathrm{rhc}} + W_{\mathrm{lhc}})$ [30] with W_{rhc} and W_{lhc}, the integrated rhc and lhc-polarized intensities in the angular range defined by NA = [0.92, 1.28]. The measurement results are shown as orange dots in Fig. 4(a). In addition, the corresponding curve retrieved from the aforementioned FDTD simulation is shown as an orange line. Numerical and experimental data are in good agreement. In Figs. 4(b)–4(d), we display the experimentally measured far-field Stokes parameter $S_3 = I_{\mathrm{rhc}} - I_{\mathrm{lhc}}$ (normalized to the maximum value of $S_0 = I_{\mathrm{rhc}} + I_{\mathrm{lhc}}$) for three selected wavelengths, where the measured average helicity is maximum, minimum, and close to zero. The minor asymmetries in the experiment, which are particularly visible in Fig. 4(c), where S_3 is relatively weak, can be attributed to the imperfect shape of the particle [see Fig. 2(c)] and small aberrations of the excitation field. In order to determine the excited dipole moments, we fit the far-field Stokes parameters of the σ dipoles, calculated with Eq. (2), to our measured data and use their complex amplitudes $A^{\pm}$ as free parameters. The theoretical far fields obtained by this method are displayed as insets in Figs. 4(b)–4(d). As an estimation for the quality of the fit, we compute the overlap integral of the fitted and the experimental electric fields, which turns out to be above 96% for all three wavelengths (see Supplement 1 for more information about the fit and the overlap integral). Adapting the formalism from Ref. [12], we calculate the chirality of the measured dipole moments:

$$C(A^{\pm}) = \frac{|A^{+}|^2 - |A^{-}|^2}{|A^{+}|^2 + |A^{-}|^2}. \tag{4}$$

The absolute squared dipole amplitudes, as well as the calculated field overlap and the chirality of the three sets of dipole moments, are listed in Table 1. Using this approach, we also determined the chirality for all measured wavelengths and show it in Fig. 4(a) as

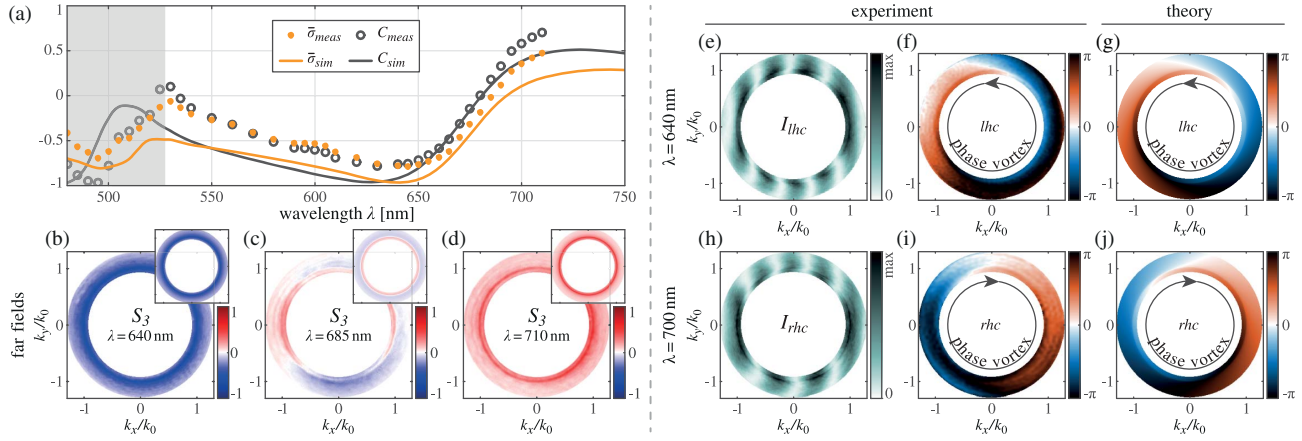

Fig. 4. (a) Spectral measurement of average helicity $\bar{\sigma}$ and chirality C depicted as orange dots and gray circles, respectively. The solid lines show corresponding results achieved by FDTD simulation. The region where the magnetic quadrupole should be taken into account for a more accurate evaluation of the chirality is shaded gray. (b)–(d) Measured BFP images showing S_3 for three different wavelengths, where $\bar{\sigma}$ is maximum, minimum, and close to zero. The images computed by fitting the far fields to the measured data are shown as insets. (e) Interference pattern of left-handed circular (lhc) polarized field, measured at 640 nm with (f) reconstructed experimental phase of the lhc polarized field component and (g) associated theoretical phase distribution for lhc field component. (h)–(j) Corresponding images for right-handed circular (rhc) polarization at 710 nm.

Table 1. Results of the Calculated Parameters

Wavelength [nm]	Field Overlap	$\lvert A^+\rvert^2$	$\lvert A^-\rvert^2$	Chirality C
640	0.98	0.12	0.88	−0.76
685	0.96	0.59	0.41	0.18
710	0.97	0.85	0.15	0.70

gray circles with a corresponding gray curve obtained by FDTD simulation. The shaded area indicates the spectral range below 530 nm, where the contribution of the magnetic quadrupole is not negligible anymore. This should be taken into account for a more precise evaluation of the chirality, where higher order multipoles are included in the analysis. Therefore, we consider the chirality to be accurate only above 530 nm.

Our experimentally reconstructed dipole moments are not exclusively σ_+ or σ_-. However, our measurements show that we are able to excite a dipole moment, which is strongly dominated by one or the other σ-dipole moment. In addition, we see that within a spectral range of only 70 nm it is possible to tune the excited dipole between two compounds of opposite dominating helicity (+ or −). The two dipole moments of maximum chirality exhibit 88% of σ_- and 85% of σ_+ for 640 and 710 nm, respectively.

For the sake of completeness, we performed simulations for a second spiral polarization beam, where the superimposed radially and azimuthally polarized beams are π out-of-phase [the in-phase superposition is depicted in Fig. 2(a)]. This change also results in a phase shift of π between the z components of the electric and magnetic fields in the focal plane. In addition, the spectra of the helicity and the chirality shown in Fig. 4(a) switches the sign [see Supplement 1, Fig. S2(c)] because the phase shift of π interchanges the handedness of the excited chiral dipole moment.

As a last step to verify the excitation of σ dipoles, we examine the conservation of angular momentum in our system. As already mentioned, our incoming beam is purely linearly polarized and, hence, carries zero SAM. Furthermore, it features a planar phase front and, therefore, also has zero OAM. However, Figs. 4(b) and 4(d) clearly reveal circular polarization in the far field scattered in the forward direction. For the purpose of angular momentum conservation in our cylindrically symmetric system [31–33], the emitted light therefore must also feature OAM of the opposite sign, which should appear as a phase vortex of $\pm 2\pi$ in the scattered light. The measured interference patterns for the lhc and rhc polarization components are shown in Figs. 4(e) and 4(h). Counting the fringes in the upper and lower half of the images, we see that for lhc polarization there is one additional fringe at the lower half, and, for rhc polarization, there is one additional fringe at the upper half, indicating opposite signs of OAM. A phase reconstruction following the technique explained in Ref. [34] results in the measured phase distributions shown in Figs. 4(f) and 4(i). The experimental phase images are in very good agreement with the theoretically calculated phase distributions [see Figs. 4(g) and 4(j)]. In particular, they prove the generation of the two phase vortices of opposite signs, which for the given wavelengths (quadrupoles and higher order multipoles can be neglected) indicate the excitation of σ-dipole moments.

6. SUMMARY

We used structured illumination with a tightly focused spiral polarization beam to excite σ-dipole moments in a spherical, achiral dielectric nanoparticle (silicon nanosphere) placed on-axis in the focal plane. Furthermore, we verified the excitation of these dipole moments by measuring their far-field helicity and OAM and investigated their spectral dependence. Our study highlights the importance of structured light in nanoscale light–matter interactions. In particular, it sheds new light on the definition of chiral dipole moments known from 3D chiral nanostructures or molecules. For such chiral building blocks, the geometry causes the excitation of a chiral dipole moment due to the mutual interaction of electric and magnetic dipole moments [18,35]. In our case, we excite a superposition of electric and magnetic dipole moments in an achiral structure in such a way that it resembles a chiral emitter [12]. The handedness is defined by the excitation field, not by the geometry of the structure.

Acknowledgment. We gratefully acknowledge fruitful discussions with Sergey Nechayev and Gerd Leuchs.

See Supplement 1 for supporting content.

REFERENCES

1. A. B. Evlyukhin, S. M. Novikov, U. Zywietz, R. L. Eriksen, C. Reinhardt, S. I. Bozhevolnyi, and B. N. Chichkov, "Demonstration of magnetic dipole resonances of dielectric nanospheres in the visible region," Nano Lett. **12**, 3749–3755 (2012).
2. L. Shi, T. U. Tuzer, R. Fenollosa, and F. Meseguer, "A new dielectric metamaterial building block with a strong magnetic response in the sub-1.5-micrometer region: silicon colloid nanocavities," Adv. Mater. **24**, 5934–5938 (2012).
3. Y. H. Fu, A. I. Kuznetsov, A. E. Miroshnichenko, Y. F. Yu, and B. Luk'yanchuk, "Directional visible light scattering by silicon nanoparticles," Nat. Commun. **4**, 1527 (2013).
4. I. Staude and J. Schilling, "Metamaterial-inspired silicon nanophotonics," Nat. Photonics **11**, 274–284 (2017).
5. P. Woźniak, P. Banzer, and G. Leuchs, "Selective switching of individual multipole resonances in single dielectric nanoparticles," Laser Photon. Rev. **9**, 231–240 (2015).
6. M. Neugebauer, P. Woźniak, A. Bag, G. Leuchs, and P. Banzer, "Polarization-controlled directional scattering for nanoscopic position sensing," Nat. Commun. **7**, 11286 (2016).
7. L. Wei, N. Bhattacharya, and H. Paul Urbach, "Adding a spin to Kerker's condition: angular tuning of directional scattering with designed excitation," Opt. Lett. **42**, 1776–1779 (2017).
8. M. F. Picardi, A. V. Zayats, and F. J. Rodríguez-Fortuño, "Janus and Huygens dipoles: near-field directionality beyond spin-momentum locking," Phys. Rev. Lett. **120**, 117402 (2018).
9. M. Neugebauer, J. S. Eismann, T. Bauer, and P. Banzer, "Magnetic and electric transverse spin density of spatially confined light," Phys. Rev. X **8**, 021042 (2018).
10. X. Zambrana-Puyalto, I. Fernandez-Corbaton, M. L. Juan, X. Vidal, and G. Molina-Terriza, "Duality symmetry and Kerker conditions," Opt. Lett. **38**, 1857–1859 (2013).
11. I. Fernandez-Corbaton and G. Molina-Terriza, "Role of duality symmetry in transformation optics," Phys. Rev. B **88**, 085111 (2013).
12. X. Zambrana-Puyalto and N. Bonod, "Tailoring the chirality of light emission with spherical Si-based antennas," Nanoscale **8**, 10441–10452 (2016).
13. L. D. Barron, *An Introduction to Chirality at the Nanoscale* (Wiley-Blackwell, 2009), Chap. 1, pp. 1–27.
14. J. K. Gansel, M. Thiel, M. S. Rill, M. Decker, K. Bade, V. Saile, G. von Freymann, S. Linden, and M. Wegener, "Gold helix photonic metamaterial as broadband circular polarizer," Science **325**, 1513–1515 (2009).
15. M. Schäferling, X. Yin, N. Engheta, and H. Giessen, "Helical plasmonic nanostructures as prototypical chiral near-field sources," ACS Photon. **1**, 530–537 (2014).

16. P. Woźniak, I. De Leon, K. Höflich, C. Haverkamp, S. Christiansen, G. Leuchs, and P. Banzer, "Chiroptical response of a single plasmonic nanohelix," arXiv: 1804.05641 (2018).
17. J. D. Jackson, *Classical Electrodynamics*, 3rd ed. (Wiley, 1999).
18. K. Y. Bliokh, Y. S. Kivshar, and F. Nori, "Magnetoelectric effects in local light-matter interactions," Phys. Rev. Lett. **113**, 033601 (2014).
19. D. O'Connor, P. Ginzburg, F. J. Rodríguez-Fortuño, G. A. Wurtz, and A. V. Zayats, "Spin-orbit coupling in surface plasmon scattering by nanostructures," Nat. Commun. **5**, 5327 (2014).
20. W. Lukosz, "Light emission by magnetic and electric dipoles close to a plane dielectric interface. III. Radiation patterns of dipoles with arbitrary orientation," J. Opt. Soc. Am. **69**, 1495–1503 (1979).
21. L. Novotny and B. Hecht, *Principles of Nano-Optics*, 2nd ed. (Cambridge University, 2006).
22. K. Youngworth and T. Brown, "Focusing of high numerical aperture cylindrical-vector beams," Opt. Express **7**, 77–87 (2000).
23. R. Alaee, M. Albooyeh, A. Rahimzadegan, M. S. Mirmoosa, Y. S. Kivshar, and C. Rockstuhl, "All-dielectric reciprocal bianisotropic nanoparticles," Phys. Rev. B **92**, 245130 (2015).
24. Y. Nakamine, T. Kodera, K. Uchida, and S. Oda, "Removal of surface oxide layer from silicon nanocrystals by hydrogen fluoride vapor etching," Jpn. J. Appl. Phys. **50**, 115002 (2011).
25. M. Decker and I. Staude, "Resonant dielectric nanostructures: a low-loss platform for functional nanophotonics," J. Opt. **18**, 103001 (2016).
26. P. Banzer, U. Peschel, S. Quabis, and G. Leuchs, "On the experimental investigation of the electric and magnetic response of a single nanostructure," Opt. Express **18**, 10905–10923 (2010).
27. L. Marrucci, C. Manzo, and D. Paparo, "Optical spin-to-orbital angular momentum conversion in inhomogeneous anisotropic media," Phys. Rev. Lett. **96**, 163905 (2006).
28. U. Mick, P. Banzer, S. Christiansen, and G. Leuchs, "AFM-based pick-and-place handling of individual nanoparticles inside an SEM for the fabrication of plasmonic nano-patterns," in *Conference on Lasers and Electro-Optics* (2014), paper STu1H.1.
29. B. Schaefer, E. Collett, R. Smyth, D. Barrett, and B. Fraher, "Measuring the Stokes polarization parameters," Am. J. Phys. **75**, 163–168 (2007).
30. A. Bekshaev, K. Y. Bliokh, and M. Soskin, "Internal flows and energy circulation in light beams," J. Opt. **13**, 053001 (2011).
31. A. Dogariu and C. Schwartz, "Conservation of angular momentum of light in single scattering," Opt. Express **14**, 8425–8433 (2006).
32. K. Y. Bliokh, J. Dressel, and F. Nori, "Conservation of the spin and orbital angular momenta in electromagnetism," New J. Phys. **16**, 093037 (2014).
33. K. Y. Bliokh, F. J. Rodríguez-Fortuño, F. Nori, and A. V. Zayats, "Spin-orbit interactions of light," Nat. Photonics **9**, 796–808 (2015).
34. M. Takeda, H. Ina, and S. Kobayashi, "Fourier-transform method of fringe-pattern analysis for computer-based topography and interferometry," J. Opt. Soc. Am. **72**, 156–160 (1982).
35. Y. Tang and A. E. Cohen, "Optical chirality and its interaction with matter," Phys. Rev. Lett. **104**, 163901 (2010).